

# Mapping cation-eutaxy ternary with a phenomenological model

Received: 8 January 2025

Accepted: 30 May 2025

Published online: 01 July 2025

 Check for updates

Jongbum Won<sup>1,2,7</sup>, Taeyoung Kim<sup>1,2,7</sup>, Minwoo Lee<sup>1,2</sup>, Daniel W. Davies<sup>3</sup>, Giyeok Lee<sup>1</sup>, Aron Walsh<sup>3</sup>, Aloysius Soon<sup>1</sup>, Jong-Young Kim<sup>4</sup> & Wooyoung Shim<sup>1,2,5,6</sup> ✉

Predicting the stability of ternary compounds poses a significant challenge due to the complex interplay of atomic features. Existing approaches often struggle to integrate these parameters into a unified framework, particularly for cation-eutaxy ABX ternary systems, where subtle compositional and bonding interactions govern the dimensionality and stability of III–V networks. To address this challenge, we developed a phenomenological model that combines electronegativity, ionic size, and charge to predict the stability and classify cation-eutaxy structures within [A–III–V] chemical systems. Our model introduces stoichiometry-weighted descriptors to evaluate the relative covalent nature of III–V and A–V bonds, bridging gaps left by traditional methodologies. Validation through computational high-throughput screening and the Materials Project database demonstrated its accuracy, successfully classifying 35 known cation-eutaxy ABX compounds and identifying 9 previously unreported candidates. As predicted by the model, experimental synthesis of  $K_2In_2P_3$  and  $Na_2In_2As_3$  confirmed the feasibility and predictive reliability of the proposed framework. While further refinements are needed, this study highlights the potential of integrating intuitive atomic features into a model for predicting cation-eutaxy ternary stability, which could lead to novel layered materials.

The prediction of equilibrium crystal structures has long been a challenge in materials science. Atomic bonding, which is determined by a variety of electronic and steric factors, governs crystal structure formation<sup>1</sup>. Among the various approaches developed, phenomenological models have been powerful tools for crystal structure prediction<sup>2</sup>. Unlike physical models that rely on costly first-principles calculations, phenomenological models are built on empirical data and excel at reproducing known results and predicting unknown phenomena<sup>3,4</sup>.

Prominent phenomenological models, such as the Hume–Rothery rules, predict the solubility and crystal structures of metallic elements

based on their atomic size and electronegativity differences<sup>5</sup>. Large electronegativity differences favor compound formation, whereas similar atomic sizes and electronegativities with small valence differences increase solubility. While these rules were primarily developed for binary metallic alloys, they may not fully capture the compositional asymmetry and charge redistribution effects observed in ternary systems. Miedema's rules<sup>6</sup>, another key model, predicted alloy formation by analyzing enthalpy changes through work function and electron density differences, favoring alloys with large work function differences and small electron density differences. Similarly, this model does not yet explicitly incorporate the electrostatic stabilization that

<sup>1</sup>Department of Materials Science and Engineering, Yonsei University, Seoul, Korea. <sup>2</sup>Center for Multi-Dimensional Materials, Yonsei University, Seoul, Korea.

<sup>3</sup>Department of Materials, Imperial College London, London, UK. <sup>4</sup>Icheon Branch, Korea Institute of Ceramic Engineering and Technology, Icheon, Korea.

<sup>5</sup>Center for Nanomedicine, Institute for Basic Science (IBS), Seoul, Korea. <sup>6</sup>Yonsei IBS Institute, Yonsei University, Seoul, Korea. <sup>7</sup>These authors contributed equally: Jongbum Won, Taeyoung Kim. ✉ e-mail: [wshim@yonsei.ac.kr](mailto:wshim@yonsei.ac.kr)

can be important for predicting stable configurations in ternary compounds.

Visualization methods, such as Villar's method<sup>7</sup> and the Mooser–Pearson plot<sup>8</sup> provide insights into the phase stability. Villar's method uses atomic size, valence, and electronegativity differences to map the AB compound stability, whereas the Mooser–Pearson plot predicts AX compound configurations based on electronegativity and atomic size, distinguishing octahedral from tetrahedral coordination. Although both approaches have been effective for binary systems, they do not fully capture the composition-sensitive bonding variations inherent to multicomponent compounds.

Pauling's rules stand out among bond polarity-based models<sup>9</sup>, defining cation (Rule 1) and anion (Rule 2) coordination numbers, cation–cation repulsion (Rule 3), and highlighting the separation of cations into distinct crystallographic planes (Rule 4), which are critical for understanding cation-eutaxy ABX ternary systems. In particular, Rule 4 is crucial for understanding the cation-eutaxy ABX ternary system, as high-valence, low-coordination cations tend to avoid polyhedral element sharing due to electrostatic repulsion. This drives the formation of layered structures with distinct cationic planes, such as  $\text{LiMnO}_2$ <sup>10</sup>, where strong cation repulsion stabilizes the layered configuration and facilitates Li-ion diffusion, a key feature in battery applications.

Cation-eutaxy ABX ternary structures are defined as layered structures in which cations preferentially occupy eutactic positions, forming a well-ordered arrangement. This structural motif, driven by strong cation-cation repulsion, has garnered significant attention as a platform for designing novel layered materials<sup>11</sup>. Topochemical etching selectively removes A-site cations from ABX ternary compounds to produce metastable BX binary layered materials<sup>12–14</sup>, thus expanding the van der Waals (vdW) library. Fewer than 100 BX binary materials have been synthesized using this method<sup>15</sup>, there is immense potential for growth in this field.

Our previous work advanced this approach by partially retaining the A-site cations to maintain structural stability, leading to layered  $\text{A}_{1-x}\text{BX}$  ternary materials<sup>16</sup>. By exploiting the A-site cation vacancies created during topochemical etching, we demonstrated memristive behavior in a class of III–V-layered semiconductors driven by a vacancy diffusion mechanism. These properties, which are absent in bulk materials, highlight the transformative potential of cationic eutaxy systems. These approaches are still in the early stages of investigation, making the identification of suitable ternary compounds an urgent research priority. Furthermore, as the study of multicomponent materials continues to gain attention, there is an increasing need for predictive models that, along with Pauling's fourth rule, can accurately assess the phase stability of ternary systems.

In this study, we present a phenomenological model to predict the stability of cation-eutaxy ABX ternary compounds. This model categorizes cationic eutaxy compounds within [A–III–V] chemical systems by assessing the covalent nature of the III–V bonds through key atomic properties, including electronegativity, ionic radius, and charge. Based on computational high-throughput screening and the Materials Project (MP) database<sup>16</sup>, we validated our proposed model using 35 known cation-eutaxy ABX compounds and nine previously unidentified candidates. Our model demonstrated high predictive accuracy by incorporating the atomic size, electronegativity, and charge. Furthermore, the experimental realization of the previously unexplored compounds,  $\text{K}_2\text{In}_2\text{P}_3$  and  $\text{Na}_2\text{In}_2\text{As}_3$ , validated the model and provided key insights for guiding the discovery of layered materials and their potential applications.

## Classification of cation-eutaxy structures

We propose a topological framework to classify ternary A–III–V compounds based on the dimensionality of the interconnected III–V polyhedra within their crystal structures (Fig. 1a). III–V compounds can

be categorized as zero-dimensional (0D), one-dimensional (1D), two-dimensional (2D), or three-dimensional (3D) III–V networks. Representative compounds are illustrated based on the crystallographic information files from the MP database<sup>17</sup>: 0D ( $\text{Ca}_{14}\text{AlSb}_{11}$ ,  $I4_1/acd$ ), 1D ( $\text{Ca}_5(\text{AlSb}_3)_2$ , *Pbam*), 2D ( $\text{CaIn}_2\text{P}_2$ ,  $P6_3/mmc$ ), and 3D ( $\text{MgB}_9\text{N}$ ,  $R\bar{3}m$ ) (see Supplementary Data 1).

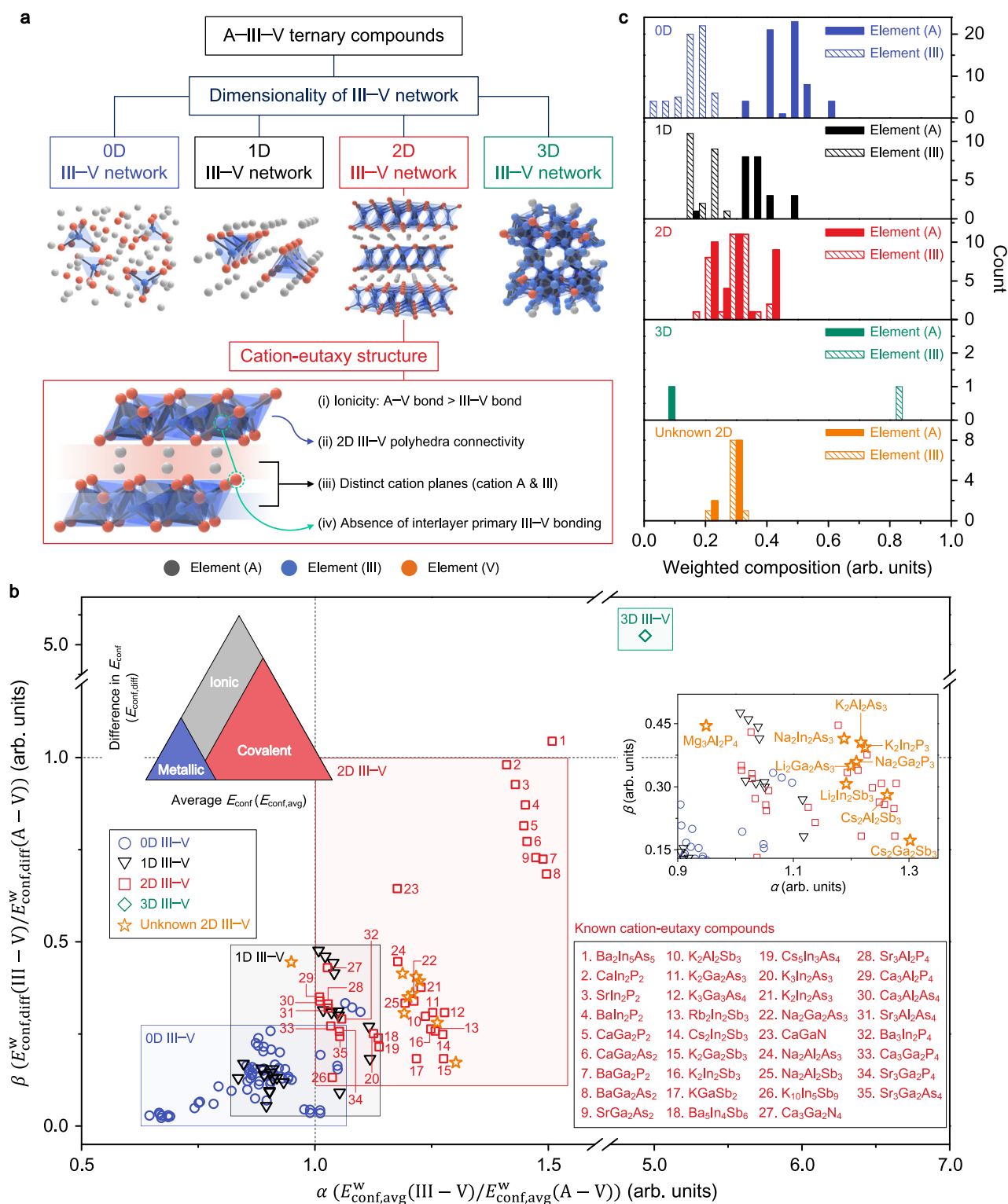
In particular, cation-eutaxy ternary compounds exhibit 2D III–V networks within their structures. These compounds are characterized by a unique cation ordering, in which cations A and III occupy separate planes to minimize electrostatic repulsion. The structural conditions defining cation-eutaxy A–III–V compounds are as follows (bottom, Fig. 1a): (1) The ionicity of the A–V bond: cation A must exhibit stronger ionic character in the A–V bond than in the III–V bond. This requires cation A to have a lower electronegativity than cation III, facilitating ionic bonding with V and strengthening the polar covalent nature of the III–V bonds. (2) Two-dimensional polyhedral connectivity: the III–V polyhedra are interconnected, similar to 2D crystals. This connectivity involves primary III–V bonding and polyanionic interactions, resulting in a layered [III–V] framework rather than a rod-like structure. (3) Distinct cation planes: cations A and III are positioned in separate planes, with the [III–V] layers sandwiched between layers composed exclusively of cation A. (4) Absence of interlayer primary bonding: along the z-axis, there are no primary bonds between the III–V polyhedra, ensuring the structural separation of the layers. These criteria allow for the effective classification of cation-eutaxy structures. Unlike conventional structures defined by specific space groups or prototypes (Supplementary Fig. 1), cation-eutaxy structures encompass various configurations across various space groups and prototypes.

In a previous study, we employed a structure-matching algorithm to identify 35 thermodynamically stable (energy above the convex hull ( $E_{\text{hull}} = 0$  eV/atom) cation-eutaxy A–III–V compounds from the MP database<sup>16</sup>. These structures were further grouped into 15 prototypes (Supplementary Fig. 2 and Supplementary Table 1). By applying an ion substitution algorithm, we identified nine additional quasi-stable ( $E_{\text{hull}} < 0.2$  eV/atom) cation-eutaxy A–III–V compounds that were not previously listed in the MP database<sup>16</sup>. This computational screening yielded 44 cation-eutaxy A–III–V compounds (Supplementary Table 1). In this study, we propose a phenomenological model and validate its accuracy using these datasets.

In ionic compounds, increasing the bond covalency often leads to the formation of more discrete structures<sup>18</sup>. Low covalency typically favors 3D close-packed structures, whereas higher covalency promotes the formation of low-dimensional architectures. Applying this principle to ternary A–III–V compounds, we hypothesized that increasing the covalency of the III–V bonds would enhance the formation of cation-eutaxy structures. To test this hypothesis, we developed models to classify cation-eutaxy compounds in [A–III–V] chemical systems by evaluating the III–V bond covalency using atomic properties such as electronegativity, ionic size, and charge. Unlike in binary systems, where bonding characteristics remain relatively constant, ternary systems exhibit composition-dependent variations due to local charge redistribution. To account for this effect, we introduced stoichiometry-weighted descriptors that systematically incorporate composition-dependent bonding variations. This analysis provides a robust framework for predicting cation-eutaxy structures and offers valuable insights for discovering layered materials through topochemical etching.

## Van Arkel-Ketelaar triangle

The van Arkel-Ketelaar triangle traditionally evaluates bonding characteristics using the average electronegativity and electronegativity difference between two elements, which classify bonding as metallic, covalent, or ionic<sup>19</sup>. However, substituting traditional electronegativity scales with the configuration energy ( $E_{\text{conf}}$ ) provides a more accurate description of the bonding characteristics<sup>20</sup>.  $E_{\text{conf}}$  is defined as the



average ionization energy of the valence electrons in the ground states<sup>21</sup> (Supplementary Fig. 3). Building on this, we utilize a modified van Arkel-Ketelaar triangle based on the average  $E_{\text{conf}}$  ( $E_{\text{conf,avg}}$ ) and  $E_{\text{conf}}$  difference ( $E_{\text{conf,diff}}$ )<sup>22</sup>.  $E_{\text{conf,avg}}$  represents the transition from metallic to covalent bonding, whereas  $E_{\text{conf,diff}}$  reflects the balance between ionic and metallic/covalent bonding (top-left inset of Fig. 1b).

We hypothesized that cation-eutaxy structures were more likely to form when the III-V network exhibited greater covalency than the A-V network. To quantitatively analyze the relative  $E_{\text{conf}}$  of the A-V and

III-V bonds in ternary compounds, we introduce a approach that incorporates stoichiometry, an aspect not previously considered in traditional van Arkel-Ketelaar triangles. This addresses the limitations of defining bond characteristics based solely on the  $E_{\text{conf}}$  of individual elements, which fails to account for the compositional influence within ternary systems.

To capture the bond characteristics more comprehensively, we propose using the stoichiometry-weighted configuration energy,  $E_{\text{conf}}^{\text{w}}$ , as a quantitative descriptor of bonding in ternary compounds.

**Fig. 1 | Topological classification of ternary A-III-V compounds based on bonding characteristics.** **a** Structure classification of A-III-V compounds according to the dimensionality of III-V network. Compounds with 0D and 1D III-V networks incorporate a 3D A-V network, whereas those with 2D III-V networks adopt alternating stacked structures with 2D A-V networks. In contrast, ternary compounds containing 3D III-V networks include 0D or 1D A-V networks. The structural conditions and representative structural schematics of cation-eutaxy structures are summarized below. **b** Phenomenological model for classifying III-V network dimensionality in ternary compounds using descriptors relative  $E_{\text{conf,avg}}^w$  ( $\alpha$ ) and relative  $E_{\text{conf,diff}}^w$  ( $\beta$ ). Bonding characteristics are quantified by  $E_{\text{conf,avg}}$  and  $E_{\text{conf,diff}}$ , displayed in a modified van Arkel-Ketelaar triangle (top left inset). Ternary

compounds with 0D, 1D, and 3D III-V networks are marked as blue circles, black inverted triangles, and green diamonds, respectively. Known cation-eutaxy compounds (2D III-V network) are represented by red squares, while unknown cation-eutaxy candidates are shown as orange stars. Regions with dense populations of specific dimensionality are shaded in corresponding background colors. Known cation-eutaxy compounds are labeled with numerical indices and their chemical formulas listed in the bottom right inset, while unknown candidates are directly labeled with their chemical formulas in the top right inset. **c** Histogram showing the composition of element A and element III in ternary compounds. Weighted compositions, calculated based on stoichiometric ratios, are represented by solid bars for element A and hatched bars for element III.

Specifically, the weighted average  $E_{\text{conf}}$  is denoted as  $E_{\text{conf,avg}}^w$  and the weighted difference is represented as  $E_{\text{conf,diff}}^w$ . These metrics were formulated for A-V and III-V bonds in  $A_l\text{III}_m\text{V}_n$ , where  $l$ ,  $m$ , and  $n$  are the stoichiometric coefficients of cations A, III, and anion V, respectively. The expressions for  $E_{\text{conf,avg}}^w$  and  $E_{\text{conf,diff}}^w$  for (A-V) and (III-V) are as follows:

$$E_{\text{conf,avg}}^w(\text{A-V}) = \frac{(l \times E_{\text{conf}}(\text{A}) + n \times E_{\text{conf}}(\text{V}))}{(l + m + n)}, \quad (1)$$

$$E_{\text{conf,avg}}^w(\text{III-V}) = \frac{(m \times E_{\text{conf}}(\text{III}) + n \times E_{\text{conf}}(\text{V}))}{(l + m + n)}, \quad (2)$$

$$E_{\text{conf,diff}}^w(\text{A-V}) = \frac{n \times l \times (E_{\text{conf}}(\text{V}) - E_{\text{conf}}(\text{A}))}{(l^2 + m^2 + n^2)}, \text{ and} \quad (3)$$

$$E_{\text{conf,diff}}^w(\text{III-V}) = \frac{n \times m \times (E_{\text{conf}}(\text{V}) - E_{\text{conf}}(\text{III}))}{(l^2 + m^2 + n^2)} \quad (4)$$

Accordingly, we define two descriptors based on the modified van Arkel-Ketelaar triangle: relative  $E_{\text{conf,avg}}^w$  ( $\alpha$ ) and relative  $E_{\text{conf,diff}}^w$  ( $\beta$ ).  $\alpha$  is calculated as the  $E_{\text{conf,avg}}^w$  of (III-V) relative to (A-V) in compounds  $A_l\text{III}_m\text{V}_n$ .  $\alpha$  is calculated as the ratio of  $E_{\text{conf,avg}}^w$  for III-V to A-V bonds:

$$\alpha = \frac{E_{\text{conf,avg}}^w(\text{III-V})}{E_{\text{conf,avg}}^w(\text{A-V})} = \frac{(m \times E_{\text{conf}}(\text{III}) + n \times E_{\text{conf}}(\text{V}))}{(l \times E_{\text{conf}}(\text{A}) + n \times E_{\text{conf}}(\text{V}))} \quad (5)$$

Similarly,  $\beta$  is calculated as:

$$\beta = \frac{E_{\text{conf,diff}}^w(\text{III-V})}{E_{\text{conf,diff}}^w(\text{A-V})} = \frac{n \times m \times (E_{\text{conf}}(\text{V}) - E_{\text{conf}}(\text{III}))}{n \times l \times (E_{\text{conf}}(\text{V}) - E_{\text{conf}}(\text{A}))} \quad (6)$$

To prevent unphysical results, such as negative  $\beta$  values or suppressed variation across compositions, we applied a weighting scheme to  $E_{\text{conf,diff}}^w$  that incorporates the product of stoichiometric coefficients and normalizes by their squared sum ( $l^2 + m^2 + n^2$ ). This formulation was essential for resolving composition-dependent bonding characteristics in ternary systems (see Methods and Supplementary Fig. 4).

Changes in  $\alpha$  reflect the transition in the metallic and covalent nature of III-V bonds compared to A-V bonds. An increase in this value indicates a stronger covalent character of the III-V bonds. Similarly, changes in  $\beta$  represent the ionic and metallic/covalent nature shift. A decrease in this value suggests that the III-V bonds exhibit a more pronounced metallic/covalent character than the A-V bonds.

Changes in  $\alpha$  and  $\beta$  play a significant role in determining the dimensionality of the III-V network (Supplementary Data 1). Specifically, an increase in  $\alpha$  drives the network transition from 0D to 3D, while a decrease in  $\beta$  shifts the network from 3D to 0D (Fig. 1b and Supplementary Fig. 5). These findings suggest a linear relationship between  $\alpha$  and  $\beta$  for the dimensionality of the network. When applied to 44 ternary A-III-V compounds, the  $\alpha$  and  $\beta$  descriptors revealed a distinct clustering of cation-eutaxy structures within a specific

parameter space. Notably, most cation-eutaxy structures were found to satisfy the criteria of  $\alpha > 1$  and  $\beta < 1$ , highlighting their strong covalent nature in III-V bonds relative to A-V bonds. This trend indicates enhanced covalency in III-V bonds when  $\alpha$  is high and  $\beta$  is low. A larger  $\alpha$  and smaller  $\beta$  correspond to stronger covalent bonding in III-V relative to A-V, thereby promoting the formation of discrete, layered III-V networks. These findings are consistent with the van Arkel-Ketelaar triangle, where increased covalency is associated with a higher  $E_{\text{conf,avg}}$  and a smaller  $E_{\text{conf,diff}}$ . Such separation was not observed when unweighted descriptors were used (Supplementary Fig. 6a), indicating that stoichiometry-weighted definitions of  $\alpha$  and  $\beta$  are essential for capturing the correlation between bonding character and structural dimensionality. Notably, the model demonstrated its robustness by accurately classifying all 35 previously known cation-eutaxy compounds and 9 newly identified ones, underscoring its potential as a reliable tool for predicting and categorizing cation-eutaxy structures.

In addition, the dimensionality of the III-V network was strongly influenced by the weighted compositions of A and III (Fig. 1c and Supplementary Data 1). First, as the composition of A decreases and that of III increases, the network transitions from 0D to 3D. Specifically, 0D III-V networks are observed when the weighted composition of A is significantly higher than that of III. In contrast, 3D networks emerge when the weighted composition of III far exceeds that of A. Second, a decrease in the weighted composition of A (i.e., low  $l$ ) and a corresponding increase in the composition of III (i.e., high  $m$ ) lead to an increase in  $\alpha$ , which enhances the covalent nature of III-V bonds and drives the transition of the network from 0D to 2D. Similarly, the trend of increasing  $\beta$  aligns with the transition from 0D to 2D, as shown in Fig. 1b. However, when  $\beta > 1$ , the network shifts to 3D, consistent with the results presented in Fig. 1b. These trends highlight how the compositional balance between A and III dictates the dimensionality of the III-V network. The descriptors,  $\alpha$ , and  $\beta$ , provide critical insights into how variations in electronegativity and composition influence the dimensionality of III-V networks, offering valuable guidance for designing and optimizing cation-eutaxy structures.

## Effective ionic radius ratio

Next, we investigated how the ionic radius influences the bonding characteristics and whether it can serve as a criterion for classifying cation-eutaxy ternary systems. According to Pauling's first rule, the ionic radius ratio ( $\frac{r_c}{r_a}$ ) between the cation and anion in a polyhedron determines the coordination number, which in turn affects bond polarization<sup>23,24</sup>. Specifically, a smaller  $\frac{r_c}{r_a}$  ratio corresponds to a lower coordination number, leading to an increase in bond polarization (top right inset of Fig. 2a). Given that bond polarization is proportional to bond covalency, the ionic radius ratio provides a means to evaluate the covalency of III-V bonds. Based on this principle, we propose a phenomenological model that utilizes the ionic radius ratio to assess the III-V bond covalency and effectively classify cation-eutaxy compounds.

First, as the ionic radius ratio ( $\frac{r_{\text{III}}}{r_{\text{V}}}$ ) decreased, the covalency of the III-V bonds increased, creating favorable conditions for the formation

of cation-eutaxy structures. Furthermore, considering that cation-eutaxy ternary systems consist of alternating layers, it is favorable for the A–V network to adopt a 2D network. Consequently, a decrease in the ionic radius ratio ( $\frac{r_A}{r_V}$ ) between cations A and V further promotes the formation of cation-eutaxy structures.

To validate this hypothesis, we also introduced weighted ionic radius ratios ( $\frac{r_A^w}{r_V^w}$  and  $\frac{r_{III}^w}{r_V^w}$ ) as descriptors, considering the stoichiometric coefficients of cations A, III, and V in the ternary compounds. The ionic radii of A, III, and V are denoted  $r_A$ ,  $r_{III}$ , and  $r_V$ , respectively<sup>25</sup>. The weighted ionic radii of A ( $r_A^w$ ), III ( $r_{III}^w$ ), and V ( $r_V^w$ ) in  $A_nIII_mV_n$  were

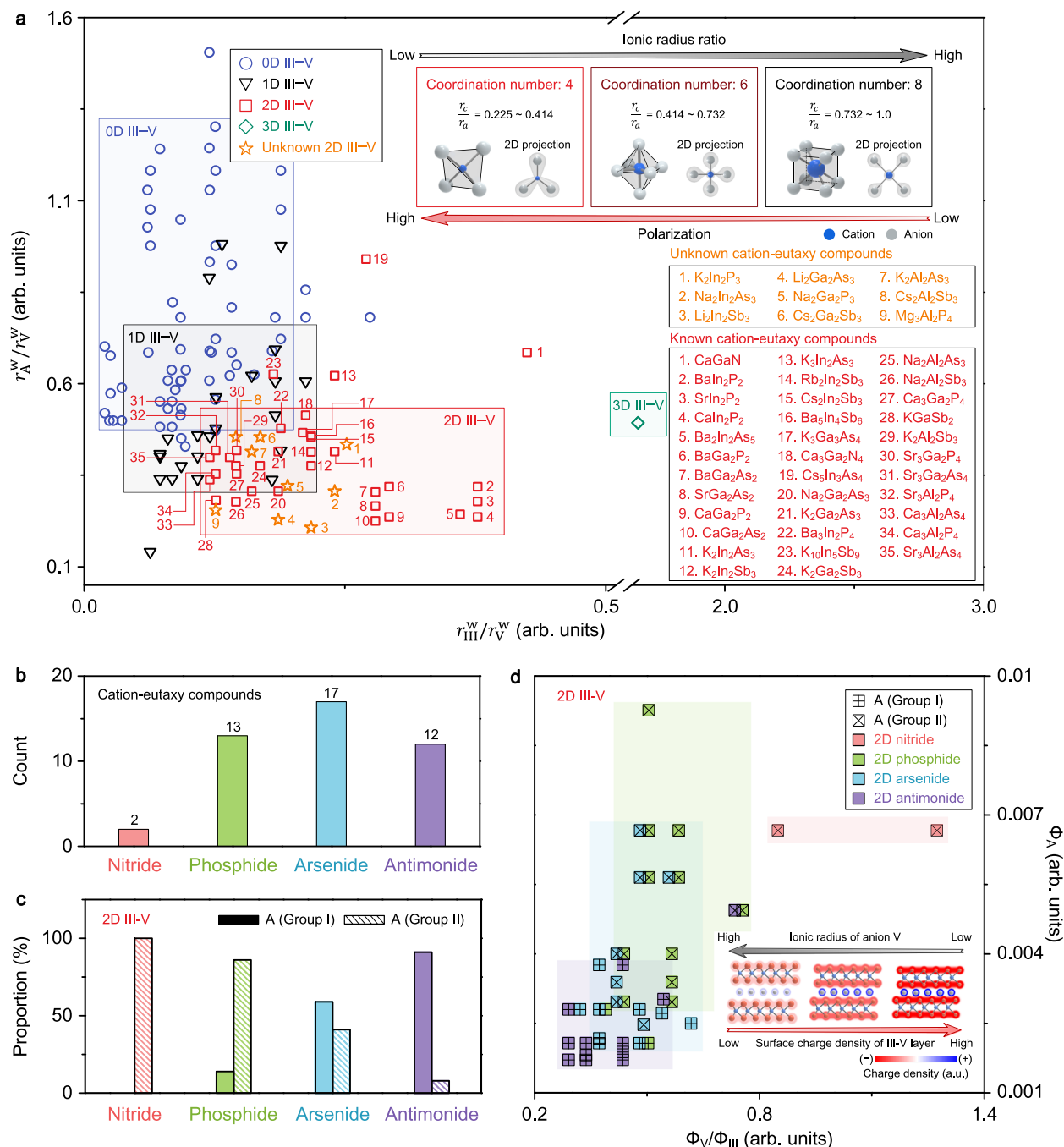


**Fig. 2 | Phenomenological model for understanding cation-eutaxy structures in ternary A–III–V compounds based on ionic radius and ionic potential.** **a** Model for classifying the dimensionality of III–V network in ternary compounds using weighted ionic radius ratios ( $\frac{r_A^w}{r_V^w}$  and  $\frac{r_{III}^w}{r_V^w}$ ). Schematic representation of polyhedral structures and corresponding electron densities in a 2D projection (top right inset). As the ionic radius ratio of the cation to the anion increases, the coordination number increases, leading to a reduction in the electron cloud overlap of ions and a decrease in polarization. Compounds with 0D, 1D, and 3D III–V networks are marked as blue circles, black inverted triangles, and green diamonds, respectively. Known cation-eutaxy compounds (2D III–V network) are represented by red squares, while unknown cation-eutaxy candidates are shown as orange stars. Regions densely populated by compounds of specific dimensionalities are

highlighted with matching background colors. Cation-eutaxy compounds are labeled numerically, with known compounds shown in red and unknown candidates in orange. The corresponding chemical formulas for each labeled compound are summarized in the bottom right inset. **b** Distribution of cation-eutaxy compounds by anion type. Nitride compounds (red) are the least common, with two examples, whereas phosphide (green), arsenide (blue), and antimonide (purple) are more prevalent, comprising 13, 17, and 12 compounds, respectively. **c** Histogram categorizing group I and II contributions to cation-eutaxy compounds, grouped by the anion V. **d** Relationship between ionic potential  $\Phi_A$  and the ratio  $\frac{\Phi_V}{\Phi_{III}}$ . Nitrides, phosphides, arsenides, and antimonides are represented in red, green, blue, and purple, respectively. The bottom right inset schematically illustrates the interplay between the surface charge density of III–V layer and the ionic radius of the anion V.

calculated as follows:

$$r_A^w = \frac{l \times r_A}{(l + m + n)}, \quad (7)$$

$$r_{III}^w = \frac{m \times r_{III}}{(l + m + n)}, \text{ and} \quad (8)$$

$$r_V^w = \frac{n \times r_V}{(l + m + n)} \quad (9)$$

The weighted ionic radius ratios are then determined as:

$$\frac{r_A^w}{r_V^w} = \frac{l \times r_A}{n \times r_V} \quad (10)$$

$$\frac{r_{III}^w}{r_V^w} = \frac{m \times r_{III}}{n \times r_V} \quad (11)$$

The analysis showed that as  $\frac{r_A^w}{r_V^w}$  decreased, the A–V network transitioned to a 2D structure. Similarly, smaller  $\frac{r_{III}^w}{r_V^w}$  values led to a reduction in the dimensionality of the III–V network, shifting from 3D to 2D, 1D, and eventually to 0D (Fig. 2a and Supplementary Data 1). This indicated an inverse relationship between  $\frac{r_A^w}{r_V^w}$  and  $\frac{r_{III}^w}{r_V^w}$  in terms of dimensionality (Fig. 2a). Overall, the dimensionality of the III–V network can be expressed as  $\frac{r_A^w}{r_V^w} \propto 1/\frac{r_{III}^w}{r_V^w}$  with clear boundaries between regions corresponding to 0D, 1D, and 2D structures (Fig. 2a and Supplementary Fig. 7). This classification was not achievable when unweighted ionic radius ratios were used (Supplementary Fig. 6b), underscoring the essential role of stoichiometry-weighted descriptors in resolving the dimensionality trends. Notably, 2D III–V networks were predominantly observed at relatively small values for both  $\frac{r_A^w}{r_V^w}$  and  $\frac{r_{III}^w}{r_V^w}$  (Fig. 2a). This finding suggests that both the III–V, and A–V networks exhibit high covalency, which is a necessary condition for attaining cation-eutaxy structures.

Analysis based on the ionic radius provides valuable insights into the selection of anions (V) necessary for the formation of cation-eutaxy structures. Specifically, we observed a striking disparity in the number of cation-eutaxy structures among the different anions: only 2 nitrides, compared to 13 phosphides, 17 arsenides, and 12 antimonides (Fig. 2b). This scarcity of nitrides can be attributed to the exceptionally small ionic radius of nitrogen, which significantly reduces the covalency of the III–V bonds, thereby increasing their ionicity. Furthermore, nitrogen's high  $E_{\text{conf}}$  appeared to contribute to the reduced covalency of the III–N bonds (Supplementary Fig. 8).

Next, we examined the role of charge in influencing the electrostatic interactions in the cation-eutaxy structure. Our analysis revealed a correlation between the ionic radius of anion V and the preference for cation A. Specifically, smaller radii of V favor the formation of cation-eutaxy structures with group II cations as A, whereas larger radii of V are associated with a preference for group I cations as A (Fig. 2c). For example, in cation-eutaxy nitrides, all the A cations belong to Group II. However, as the ionic radius of V increases from phosphorus to Sb, the proportion of group I cations in A increases, culminating in antimonides, where A predominantly consists of group I cations. This relationship can be attributed to the balance between the electrostatic repulsion within the 2D III–V networks and the shielding effect the A cations provide in the cation-eutaxic A–III–V structures (bottom-right inset of Fig. 2d). In 2D III–V networks, the anion V is positioned on the surface and carries surface charges, whereas cation A is situated between the III–V layers, maintaining structural stability. An analysis of the ionic potential ( $\Phi$ ), which represents the charge density at the

surface of an ion, demonstrates that the balance between electrostatic repulsion across III–V layers and the shielding effect of A is critical for forming cation-eutaxy structures.

The ionic potential ( $\Phi_i$ ) of an ion can be defined as  $\frac{w_i \times n_i}{r_i}$ , where  $w_i$  represents the content of ion i,  $n_i$  is the charge, and  $r_i$  is the ionic radius<sup>26</sup>. We note that this heuristic is associated with the effective potential of an ion's electrostatic influence, rather than a direct physical potential. As  $\Phi_V$  increases and  $\Phi_{III}$  decreases, the high charge density of anion V becomes concentrated on the surface of the layer, leading to an increase in the surface charge density of the III–V layers. Consequently, a higher  $\frac{\Phi_V}{\Phi_{III}}$  ratio results in a greater negative charge on the layer surface, amplifying the electrostatic repulsion between the III–V layers. Conversely, an increase in  $\Phi_A$  enhances the shielding effect of cation A, counteracting this repulsion<sup>27</sup>. As shown in Fig. 2d, a clear proportional relationship exists between  $\frac{\Phi_V}{\Phi_{III}}$  and  $\Phi_A$  in cation-eutaxy A–III–V structures (Supplementary Table 1). This relationship underscores the critical role of sufficient shielding by cation A in stabilizing the III–V layers when the surface charge density is high.

### Unknown cation-eutaxy within $A_2In_2V_3$ prototype system

In the previous analysis, cation-eutaxy structures were classified based on atomic features, and surface charge considerations determined the preference for the specific cations A. Building on this, we integrated electronegativity, ionic radius, and charge into a unified classification framework.

We focused on the  $A_2III_2V_3$  prototype structures (top left inset of Fig. 3a) within the [A–In–V] chemical space, where indium serves as a group-III element. Among the 15 prototype structures identified across the 44 predicted cation-eutaxy compounds, the  $A_2III_2V_3$  type was the most frequently encountered, with In-based compositions comprising the largest subset. We therefore selected the  $A_2In_2V_3$  system as a representative case for validating the predictive power of the model through experimental synthesis. The results revealed the following key findings by plotting cation-eutaxy  $A_2In_2V_3$  compounds using the relative  $E_{\text{conf, diff}}^w$  ( $\beta$ ), and the weighted ionic radius ratio of In over V ( $\frac{r_{In}^w}{r_V^w}$ ). First, we identified clear boundaries between cation-eutaxy and non-cation-eutaxy structures at  $\beta = 0.42$  and  $\frac{r_{In}^w}{r_V^w} = 0.26$  (Fig. 3a and Supplementary Table 2). In  $A_2In_2V_3$  cation-eutaxy structures, charge neutrality requires cation A to be an alkali metal. However, for  $A_2In_2N_3$ , the high  $\frac{\Phi_N}{\Phi_{In}}$  ratio results in significant electrostatic repulsion between  $In_2N_3$  layers, necessitating a cation A with high  $\Phi_A$ , such as those found in alkaline earth metals, to provide sufficient shielding. As a result,  $A_2In_2N_3$  structures with alkali metal cations are structurally unstable and classified as non-cation-eutaxy structures. Third, our analysis confirms that lower  $\beta$  and  $\frac{r_{In}^w}{r_V^w}$  values favor the formation of cation-eutaxy  $A_2In_2V_3$ . These results highlight the effectiveness of using an integrated approach combining electronegativity, ionic radius, and charge to classify cation-eutaxy structures and provide strong evidence for the feasibility and accuracy of the proposed phenomenological model.

We further investigated structural stability by calculating the formation enthalpies (Fig. 3b). For example, in the transitions from  $Na_2In_2Sb_3$  ( $E_{\text{hull}} = 0.010$  eV/atom) to  $Na_2In_2As_3$  ( $E_{\text{hull}} = 0.043$  eV/atom) and from  $K_2In_2As_3$  ( $E_{\text{hull}} = 0.0$  eV/atom) to  $K_2In_2P_3$  ( $E_{\text{hull}} = 0.022$  eV/atom), we observed a trend of increasing  $E_{\text{hull}}$  as the size of anion V decreased. Similarly, when  $K_2In_2Sb_3$  ( $E_{\text{hull}} = 0.0$  eV/atom) and  $K_2In_2As_3$  ( $E_{\text{hull}} = 0.0$  eV/atom) were replaced by  $Li_2In_2Sb_3$  ( $E_{\text{hull}} = 0.197$  eV/atom) and  $Na_2In_2As_3$  ( $E_{\text{hull}} = 0.043$  eV/atom), respectively, a smaller cation A was associated with a higher  $E_{\text{hull}}$ . This increase in the formation enthalpy indicates reduced thermodynamic stability, adversely affecting the formation of the cation-eutaxy structure. These trends align with the relationships depicted in Fig. 3a, where  $\beta$  and  $\frac{r_{In}^w}{r_V^w}$  are inversely proportional to stability. For instance,  $K_2In_2As_3$  is classified as a stable, known cation-eutaxy structure, whereas  $Na_2In_2As_3$  is

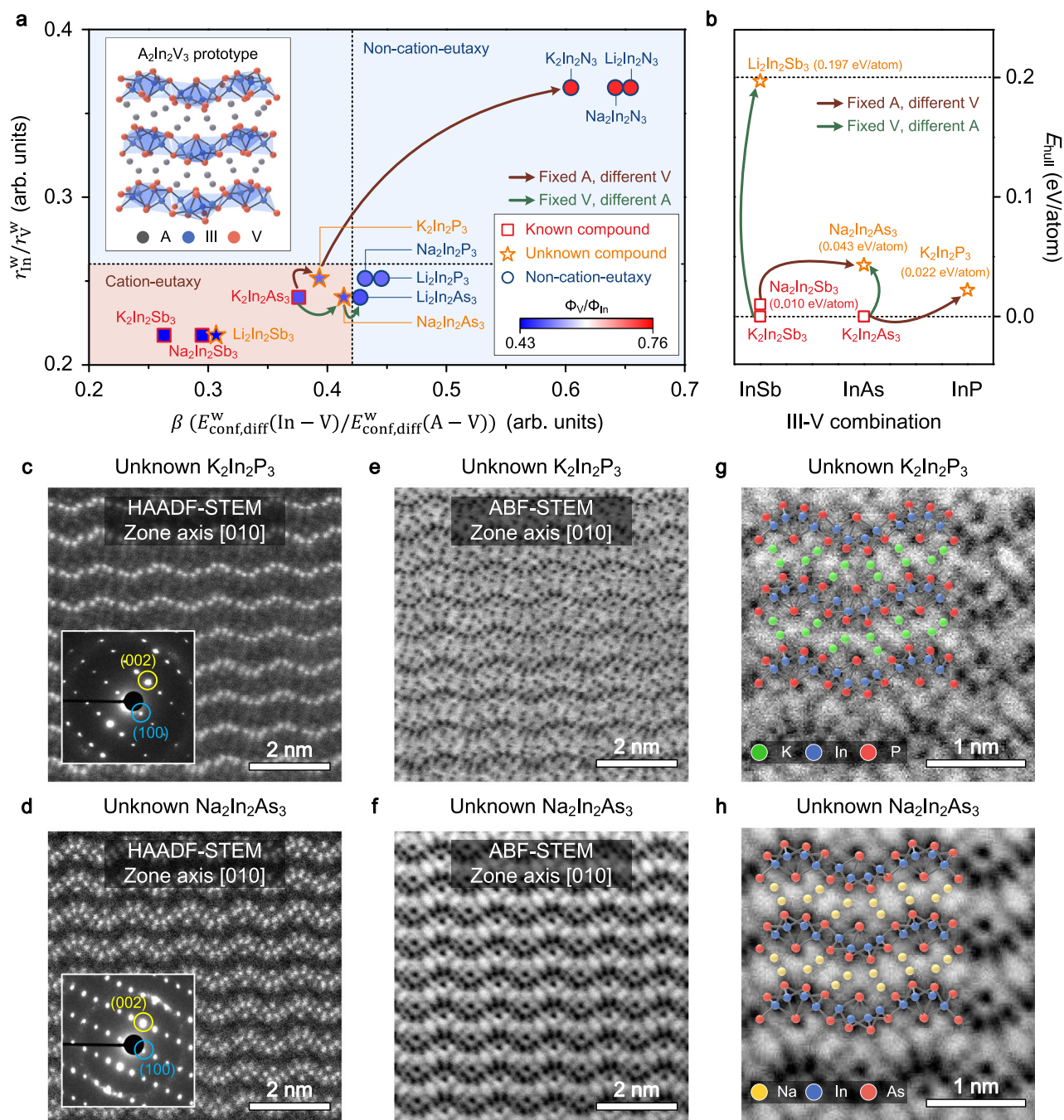


**Fig. 3 | Discovery of unknown  $K_2In_2P_3$  and  $Na_2In_2As_3$  compounds.** **a** Combined phenomenological model for  $[A_2-In_2-V_3]$  chemical systems. The background color highlights distinct regions of predicted structural behavior: the blue area corresponds to non-cation-eutaxy compounds, while the brown area encompasses the predicted cation-eutaxy region, including both known and unknown candidates. The top left inset shows a simulated image of a representative cation-eutaxy  $A_2In_2V_3$  structure, generated from a crystallographic information file. **b** Thermodynamic stability of cation-eutaxy compounds within this family, with  $E_{hull}$  values of  $Li_2In_2Sb_3$ ,  $Na_2In_2Sb_3$ ,  $K_2In_2Sb_3$ ,  $Na_2In_2As_3$ ,  $K_2In_2As_3$ , and  $K_2In_2P_3$  calculated as 0.197,

0.010, 0.000, 0.043, 0.000, and 0.022 eV/atom, respectively. The variations in  $E_{hull}$  due to ion substitution of anion V and cation A are highlighted with brown and green arrows, respectively. **c, d** HAADF-STEM images and corresponding SAED patterns (insets) of  $K_2In_2P_3$  (**c**) and  $Na_2In_2As_3$  (**d**), viewed along the [010] zone axis. The electron diffraction patterns of (002) and (100) are indexed by yellow and blue circles, respectively. **e, f** ABF-STEM images of  $K_2In_2P_3$  (**e**) and  $Na_2In_2As_3$  (**f**) along the [010] zone axis. **g, h** Enlarged ABF-STEM images of  $K_2In_2P_3$  (**g**) and  $Na_2In_2As_3$  (**h**) showing agreement with crystallographic information file-based structural models.

metastable, and  $Li_2In_2As_3$  is a non-cation-eutaxy structure. Similarly,  $K_2In_2As_3$  has a stable cation-eutaxy structure,  $K_2In_2P_3$  is metastable, and  $K_2In_2N_3$  has a non-cation-eutaxy structure. In conclusion, substituting cations A and V with smaller ions reduces the likelihood of the formation of cation-eutaxy structures.

To rigorously assess the reliability of our model, we selected  $K_2In_2P_3$  and  $Na_2In_2As_3$ , which were identified as candidate cation-

eutaxy compounds with  $\beta$  and  $r_{In}^w/r_V^w$  values near the classification threshold. This selection allowed us to evaluate the model's accuracy in distinguishing cation-eutaxy from non-cation-eutaxy compounds. Plate-shaped  $K_2In_2P_3$  and  $Na_2In_2As_3$ , synthesized via solid-state methods, were characterized using scanning electron microscopy (SEM), which confirmed their morphologies (Supplementary Fig. 9). The elemental composition of  $K_2In_2P_3$  and  $Na_2In_2As_3$  was confirmed through

energy-dispersive spectroscopy (EDS) analysis (Supplementary Fig. 9). X-ray diffraction (XRD) analysis further demonstrated that these compounds possessed crystal structures identical to those predicted by the simulated structures (Supplementary Fig. 10). The calculated XRD patterns were derived from ion substitution algorithm-predicted structures and relaxed using generalized gradient approximation (GGA)<sup>28</sup>. To resolve the atomic structures precisely, scanning transmission electron microscopy (STEM) analysis was performed on both unknown compounds. High-angle annular dark-field STEM (HAADF-STEM) imaging using focused ion beam (FIB)-prepared specimens revealed distinct atomic arrangements of the  $\text{In}_2\text{P}_3$  and  $\text{In}_2\text{As}_3$  layers, consistent with cation-eutaxy  $\text{A}_2\text{III}_2\text{V}_3$  structures (Fig. 3c, d). Additionally, selected-area electron diffraction (SAED) patterns confirmed that  $\text{K}_2\text{In}_2\text{P}_3$  and  $\text{Na}_2\text{In}_2\text{As}_3$  exhibited monoclinic P-lattice symmetry (insets in Fig. 3c, d). To ensure the accurate detection of light elements such as K and Na, annular bright-field STEM (ABF-STEM) analysis was conducted, which unequivocally confirmed that the synthesized compounds aligned perfectly with the atomic arrangements predicted for cation-eutaxy  $\text{A}_2\text{III}_2\text{V}_3$  structures (Fig. 3e–h).

Furthermore, we attempted to synthesize  $\text{Li}_2\text{In}_2\text{P}_3$ ,  $\text{Li}_2\text{In}_2\text{As}_3$ , and  $\text{Na}_2\text{In}_2\text{P}_3$ , which exhibited  $\beta$  and  $\frac{r_{\text{III}}^{\text{w}}}{r_{\text{V}}^{\text{w}}}$  values similar to  $\text{K}_2\text{In}_2\text{P}_3$  and  $\text{Na}_2\text{In}_2\text{As}_3$  but were classified as non-cation-eutaxy compounds (Supplementary Fig. 11). XRD analysis revealed that the synthesized materials consisted of zinc-blende III–V phases along with either a ternary phase with a non-cation-eutaxy structure or highly reactive binary phases, depending on the chemical system. This outcome strongly supports the validity of the descriptor threshold established for distinguishing cation-eutaxy structures within the  $\text{A}_2\text{In}_2\text{V}_3$  family, reinforcing the predictive power of our model.

Our phenomenological model proved to be effective in classifying cation-eutaxy structures, as its predictions were consistent with experimental observations and aligned with the results of the ion substitution algorithm. This model introduces a threshold for distinguishing cation-eutaxy from non-cation-eutaxy structures, which cannot be derived using the ion substitution algorithm alone. Materials falling outside this threshold can be excluded from consideration as cation-eutaxy compounds, thus streamlining future high-throughput screening efforts. The complementary use of high-throughput screening and a phenomenological model offers a highly efficient pathway for identifying promising cation-eutaxy structures.

In this study, we developed a phenomenological model to classify cation-eutaxy compounds based on the following key parameters: electronegativity, ionic radius, and charge. Our model demonstrated a high level of agreement with the results obtained from high-throughput screening methods that combined ion substitution algorithms and formation energy calculations.

This study provides insight into the atomic properties that govern the formation of cation-eutaxy structures in ternary compounds, deepening our understanding of the fundamental factors influencing these arrangements. Moreover, the approach can be extended to other prototype structures suitable for topochemical etching, offering a framework for the synthesis of additional families of 2D materials. The current model is particularly effective for compounds composed of s- and p-block elements, but may be less applicable to systems involving transition metals, where d-orbital interactions and crystal field effects play a significant role in structural stability (Supplementary Fig. 12 and Supplementary Table 3). In addition, because the model does not explicitly incorporate thermodynamic parameters, it does not provide direct information on thermodynamic stability. Despite these limitations, the integration of atomic-scale understanding with predictive modeling contributes to the rational design of cation-eutaxy structures and their potential applications.

## Methods

### Computational screening for cation-eutaxy structures

To classify the III–V network dimensionality in ternary compounds, we employed a structure matching algorithm implemented in the Pymatgen Python library<sup>17</sup>. A dataset of 35 cation-eutaxy compounds was obtained from the Materials Project database<sup>29</sup> and analyzed using the structure matching algorithm with a fractional length tolerance of 0.2 and site tolerance of 0.3, yielding 19 unique prototype structures.

To predict unknown cation-eutaxy structures, we employed an ionic substitution algorithm<sup>30</sup> leveraging a data-driven statistical model trained on known compounds. This model assigns probabilities to element substitutions based on oxidation states and chemical environments, enabling targeted predictions of stable ternary compounds. The substitutions were validated based on a probability threshold of  $1 \times 10^{-8}$  and common oxidation states defined in the Smact library<sup>31</sup>. This methodology, originally trained on pnictide compounds, was implemented using Pymatgen's substitution framework<sup>32</sup>, further enhancing the prediction accuracy of potential cation-eutaxy structures.

The structural refinement and validation of the predicted compounds were performed using density functional theory (DFT) calculations within the Vienna Ab initio Simulation Package (VASP) framework. Energy minimization and lattice relaxation were conducted using projector-augmented wave (PAW) potentials<sup>33–35</sup>, with the PBE exchange-correlation functional applied following the calculation settings specified in the Materials Project<sup>28</sup>.

The stability of each predicted cation-eutaxy structure was assessed via  $E_{\text{hull}}$  calculations using the PhaseDiagram API from Pymatgen<sup>32,36,37</sup>. A metastability tolerance of 200 meV/atom above the convex hull was applied, ensuring that only thermodynamically reasonable structures were considered.

All calculations were performed using publicly available open-source tools, ensuring reproducibility. Computational workflows, including structure-matching algorithms, ionic substitution models, and phase stability analyses, are fully documented and accessible via the Pymatgen and Smact libraries.

### Descriptor formulation and weighting scheme

To quantitatively capture bonding characteristics in ternary A–III–V compounds, we introduced stoichiometry-weighted descriptors based on  $E_{\text{conf}}$  and ionic radius. The stoichiometric ratios of constituent elements were systematically incorporated into the descriptor definitions to reflect composition-dependent variations in bonding behavior.

For the  $E_{\text{conf, avg}}^{\text{w}}$  and  $r^{\text{w}}$ , each elemental property was scaled by its stoichiometric coefficient normalized by the total number of atoms in the formula unit ( $l + m + n$ ). For example, in a compound with the composition  $\text{A}_l\text{III}_m\text{V}_n$ , the weighted configuration energy and weighted ionic radius of cation A are defined as

$$E_{\text{conf}}^{\text{w}}(\text{A}) = \frac{l}{(l + m + n)} E_{\text{conf}}(\text{A}), \quad r_{\text{A}}^{\text{w}} = \frac{l}{(l + m + n)} r_{\text{A}}$$

Based on these values,  $E_{\text{conf, avg}}^{\text{w}}$  for A–V and III–V bonds were calculated as follows:

$$E_{\text{conf, avg}}^{\text{w}}(\text{A} - \text{V}) = \frac{l \times E_{\text{conf}}(\text{A}) + n \times E_{\text{conf}}(\text{V})}{(l + m + n)},$$

$$E_{\text{conf, avg}}^{\text{w}}(\text{III} - \text{V}) = \frac{m \times E_{\text{conf}}(\text{III}) + n \times E_{\text{conf}}(\text{V})}{(l + m + n)}$$

In contrast,  $E_{\text{conf, diff}}^{\text{w}}$  required a different scheme to resolve issues such as negative descriptor values and poor resolution across compositions. To address this, we incorporated the product of relevant

stoichiometric coefficients and normalized by the sum of squared coefficients ( $l^2 + m^2 + n^2$ ). For instance,  $E_{\text{conf,diff}}^{\text{W}}$  for A–V and III–V bonds were expressed as:

$$E_{\text{conf,diff}}^{\text{W}}(\text{A} - \text{V}) = \frac{n \times l \times (E_{\text{conf}}(\text{V}) - E_{\text{conf}}(\text{A}))}{(l^2 + m^2 + n^2)},$$

$$E_{\text{conf,diff}}^{\text{W}}(\text{III} - \text{V}) = \frac{n \times m \times (E_{\text{conf}}(\text{V}) - E_{\text{conf}}(\text{III}))}{(l^2 + m^2 + n^2)}$$

Final bonding descriptors were then defined as relative metrics:

$$\alpha = \frac{E_{\text{conf,avg}}^{\text{W}}(\text{III}-\text{V})}{E_{\text{conf,avg}}^{\text{W}}(\text{A}-\text{V})}, \beta = \frac{E_{\text{conf,diff}}^{\text{W}}(\text{III}-\text{V})}{E_{\text{conf,diff}}^{\text{W}}(\text{A}-\text{V})}$$

This combined weighting strategy enabled consistent prediction and classification of III–V network dimensionality across a broad range of ternary compositions, by capturing subtle variations in bonding asymmetry and charge distribution that are not accessible using unweighted descriptors.

### Preparation of unknown $\text{K}_2\text{In}_2\text{P}_3$

$\text{K}_2\text{In}_2\text{P}_3$  was synthesized using a solid-state method in an inert atmosphere to prevent the alkali metals from reacting with moisture and oxygen. A mixture of 0.195 g of bulk potassium (Thermo Fisher Scientific, chunks in mineral oil, 98%), 0.574 g of indium shot (Thermo Fisher Scientific, teardrops (4 mm), 99.99%), and 0.232 g of red phosphorus lumps (Thermo Fisher Scientific, lumps, 99.999 + %) was placed in an alumina crucible, which was then sealed inside a quartz ampoule. The ampoule was heated in a programmable furnace to 750 °C for 3 h, held at 750 °C for 20 h, cooled to 500 °C in 50 h, maintained at 500 °C for 100 h, and finally cooled to room temperature in 100 h. After the reaction, the quartz ampoule was broken under argon atmosphere to retrieve the crystals, which were then washed with methanol to remove the byproducts.

### Preparation of unknown $\text{Na}_2\text{In}_2\text{As}_3$

$\text{Na}_2\text{In}_2\text{As}_3$  was synthesized by reacting stoichiometric amounts of bulk sodium (Thermo Fisher Scientific, ingot, 99.8%), indium shots (Thermo Fisher Scientific, teardrop (4 mm), 99.99%), and arsenic powder (Thermo Fisher Scientific, lump, 99.999%) in a 2:2:3 molar ratio. The materials were placed in an alumina crucible and subsequently loaded into a quartz ampoule inside an Ar-filled glove box. The ampoule was sealed under an argon atmosphere using the double-ampoule technique to prevent oxidation, with the smaller ampoule inside the larger one. The sealed ampoule was heated in a box furnace at a rate of 100 °C/h to 1000 °C and held at this temperature for 4 h. Afterward, the temperature decreased from 1000 to 500 °C at a rate of 5 °C/h, and the sample was maintained at 500 °C for 100 h to facilitate crystal growth. The ampoule was then allowed to cool naturally in a furnace. The resulting  $\text{Na}_2\text{In}_2\text{As}_3$  crystals exhibited a powdery morphology, with a typical particle size of approximately 0.1 mm and a gray color.

### Reporting summary

Further information on research design is available in the Nature Portfolio Reporting Summary linked to this article.

### Data availability

The data supporting the findings of this study are available in publicly accessible repositories and databases. The dataset of 35 cation-eutaxy compounds used for structural screening was obtained from the Materials Project database (<https://materialsproject.org>). The computational workflows, including structure-matching algorithms, ionic substitution models, and phase stability analyses, were implemented using open-source libraries such as Pymatgen (<https://pymatgen.org>)

and Smact (<https://github.com/WMD-group/Smact>), ensuring full reproducibility. Convex hull stability calculations were performed using the PhaseDiagram API within Pymatgen. The parameters and methodologies for DFT calculations follow the protocols outlined in the Materials Project documentation. Source data are provided with this paper.

### References

- Pauling, L. The principles determining the structure of complex ionic crystals. *J. Am. Chem. Soc.* **51**, 1010–1026 (1929).
- Pauling, L. *The Nature of the Chemical Bond and the Structure of Molecules and Crystals: An Introduction to Modern Structural Chemistry* (Cornell University Press, 1960).
- Pettifor, D. G. A chemical scale for crystal-structure maps. *Solid State Commun* **51**, 31–34 (1984).
- Zunger, A. Systematization of the stable crystal structure of all ab-type binary compounds: a pseudopotential orbital-radii approach. *Phys. Rev. B* **22**, 5839–5872 (1980).
- G. V. Rothery, W. H. & R. *The Structure of Metals and Alloys* (The Institute of Metals, 1956).
- Miedema, A. R. Simple model for alloys. *Philips Tech Rev* **33**, 149–160 (1973).
- Villars, P. A three-dimensional structural stability diagram for 998 binary ab intermetallic compounds. *J. Common Met.* **92**, 215–238 (1983).
- Mooser, E. & Pearson, W. B. On the crystal chemistry of normal valence compounds. *Acta Crystallogr* **12**, 1015–1022 (1959).
- Pauling, L. The nature of the chemical bond. iv. the energy of single bonds and the relative electronegativity of atoms. *J. Am. Chem. Soc.* **54**, 3570–3582 (1932).
- Armstrong, A. R. & Bruce, P. G. Synthesis of layered  $\text{LiMnO}_2$  as an electrode for rechargeable lithium batteries. *Nature* **381**, 499–500 (1996).
- Shim, W. An approach to identify and synthesize memristive iii–v semiconductors. *Nat. Mater.* **23**, 1322–1323 (2024).
- Won, J. et al. Polytropic two-dimensional feases with high anisotropy. *Nano Lett* **23**, 11057–11065 (2023).
- Xiao, X., Wang, H., Urbankowski, P. & Gogotsi, Y. Topochemical synthesis of 2D materials. *Chem. Soc. Rev.* **47**, 8744–8765 (2018).
- Zhang, Q., Peng, W., Li, Y., Zhang, F. & Fan, X. Topochemical synthesis of low-dimensional nanomaterials. *Nanoscale* **12**, 21971–21987 (2020).
- Bae, J. et al. Kinetic 2D crystals via topochemical approach. *Adv. Mater.* **33**, 2006043 (2021).
- Bae, J. et al. Cation-Eutaxy-Enabled III–V-Derived van Der Waals Crystals as Memristive Semiconductors. *Nat. Mater.* **23**, 1402–1410 (2024).
- Jain, A. et al. Commentary: the materials project: a materials genome approach to accelerating materials innovation. *APL Mater* **1**, 011002 (2013).
- Rohrer, G. S. *Structure and Bonding in Crystalline Materials* (Cambridge University Press, 2001).
- Arkel, A. E. V. *Molecules and Crystals in Inorganic Chemistry* (Butterworths Scientific, 1994).
- Sproul, G. Electronegativity and Bond Type. 2. Evaluation of Electronegativity Scales. *J. Phys. Chem.* **98**, 6699–6703 (1994).
- Mann, J. B., Meek, T. L. & Allen, L. C. Configuration energies of the main group elements. *J. Am. Chem. Soc.* **122**, 2780–2783 (2000).
- Allen, L. C., Capitani, J. F., Kolks, G. A. & Sproul, G. D. Van Arkel–Ketelaar Triangles. *J. Mol. Struct.* **300**, 647–655 (1993).
- Allen, L. C. Electronegativity is the average one-electron energy of the valence-shell electrons in ground-state free atoms. *J. Am. Chem. Soc.* **111**, 9003–9014 (1989).
- Greenwood, N. N. *Ionic Crystals, Lattice Defects and Non-stoichiometry* (Butterworths: London, 1968).

25. Shannon, R. D. Revised effective ionic radii and systematic studies of interatomic distances in halides and chalcogenides. *Acta Crystallogr. Sect. A* **32**, 751–767 (1976).
26. Cartledge, G. H. Studies on the periodic system. i. the ionic potential as a periodic function<sup>1</sup>. *J. Am. Chem. Soc.* **50**, 2855–2863 (1928).
27. Zhao, C. et al. Rational design of layered oxide materials for sodium-ion batteries. *Science* **370**, 708–711 (2020).
28. Perdew, J. P., Burke, K. & Ernzerhof, M. Generalized gradient approximation made simple. *Phys. Rev. Lett.* **77**, 3865–3868 (1996).
29. Ong, S. P. et al. The materials application programming interface (api): a simple, flexible and efficient api for materials data based on representational state transfer (REST) Principles. *Comput. Mater. Sci.* **97**, 209–215 (2015).
30. Hautier, G., Fischer, C., Ehrlicher, V., Jain, A. & Ceder, G. Data Mined Ionic Substitutions for the Discovery of New Compounds. *Inorg. Chem.* **50**, 656–663 (2011).
31. Davies, D. W. et al. SMACT: semiconducting materials by analogy and chemical theory. *J. Open Source Softw.* **4**, 1361 (2019).
32. Ong, S. P. et al. Python materials genomics (Pymatgen): a robust, open-source python library for materials analysis. *Comput. Mater. Sci.* **68**, 314–319 (2013).
33. Kresse, G. & Joubert, D. From ultrasoft pseudopotentials to the projector augmented-wave method. *Phys. Rev. B* **59**, 1758–1775 (1999).
34. Kresse, G. & Furthmüller, J. Efficiency of Ab-Initio total energy calculations for metals and semiconductors using a plane-wave basis set. *Comput. Mater. Sci.* **6**, 15–50 (1996).
35. Kresse, G. & Hafner, J. Ab Initio molecular dynamics for open-shell transition metals. *Phys. Rev. B* **48**, 13115–13118 (1993).
36. Ong, S. P., Wang, L., Kang, B. & Ceder, G. Li–Fe–P–O<sub>2</sub> Phase diagram from first principles calculations. *Chem. Mater.* **20**, 1798–1807 (2008).
37. Ong, S. P., Jain, A., Hautier, G., Kang, B. & Ceder, G. Thermal Stabilities of Delithiated Olivine MPO<sub>4</sub> (M=Fe, Mn) cathodes investigated using first principles calculations. *Electrochem. Commun.* **12**, 427–430 (2010).

## Acknowledgements

This work was supported by the Nano & Material Technology Development Program through the National Research Foundation (NRF) of Korea funded by the Ministry of Science and ICT (RS-2024-00468995, J. W., T. K., M. L., G. L., A. S., J. K., and W.S.) and a grant from the Institute for Basic Science (IBS-R026-D1, W.S.). We are grateful to the UK Materials and Molecular Modeling Hub for computational resources, which is partially funded by EPSRC (EP/TO22213/1, EP/W032260/1 and EP/PO20194/1, D.W.D. and A.W.).

## Author contributions

J. W., T. K., M.L., J.K., and W.S. developed the phenomenological model. J.W. and T.K. synthesized the materials and conducted the structural analysis. G.L. and A.S. performed the first-principles calculations and analyses, while D. W. D. and A.W. developed the data-driven models. All authors wrote the manuscript and contributed to the overall scientific interpretation.

## Competing interests

The authors declare no competing interests.

## Additional information

**Supplementary information** The online version contains supplementary material available at <https://doi.org/10.1038/s41467-025-60739-9>.

**Correspondence** and requests for materials should be addressed to Wooyoung Shim.

**Peer review information** *Nature Communications* thanks Wen Tong, Lijun Zhang and the other, anonymous, reviewer(s) for their contribution to the peer review of this work. A peer review file is available.

**Reprints and permissions information** is available at <http://www.nature.com/reprints>

**Publisher's note** Springer Nature remains neutral with regard to jurisdictional claims in published maps and institutional affiliations.

**Open Access** This article is licensed under a Creative Commons Attribution-NonCommercial-NoDerivatives 4.0 International License, which permits any non-commercial use, sharing, distribution and reproduction in any medium or format, as long as you give appropriate credit to the original author(s) and the source, provide a link to the Creative Commons licence, and indicate if you modified the licensed material. You do not have permission under this licence to share adapted material derived from this article or parts of it. The images or other third party material in this article are included in the article's Creative Commons licence, unless indicated otherwise in a credit line to the material. If material is not included in the article's Creative Commons licence and your intended use is not permitted by statutory regulation or exceeds the permitted use, you will need to obtain permission directly from the copyright holder. To view a copy of this licence, visit <http://creativecommons.org/licenses/by-nc-nd/4.0/>.

© The Author(s) 2025